Electrical tuning of the magnetic properties of two-dimensional magnets: Cr$_2$Ge$_2$Te$_6$

Guido Menichetti [1,2,*] Matteo Calandra [3,2,4] and Marco Polini [1,5]

[1]*Dipartimento di Fisica dell'Universitá di Pisa, Largo Bruno Pontecorvo 3, I-56127 Pisa, Italy*
[2]*Istituto Italiano di Tecnologia, Graphene Labs, Via Morego 30, I-16163 Genova, Italy*
[3]*Department of Physics, University of Trento, Via Sommarive 14, 38123 Povo, Italy*
[4]*Sorbonne Université, CNRS, Institut des Nanosciences de Paris, UMR7588, F-75252 Paris, France*
[5]*ICFO-Institut de Ciències Fotòniques, The Barcelona Institute of Science and Technology,*
Av. Carl Friedrich Gauss 3, 08860 Castelldefels (Barcelona), Spain

Motivated by growing interest in atomically thin van der Waals magnetic materials, we present an *ab initio* theoretical study of the dependence of their magnetic properties on the electron/hole density ρ induced via the electrical field effect. By focusing on the case of monolayer Cr$_2$Ge$_2$Te$_6$ (a prototypical 2D Ising ferromagnet) and employing a hybrid functional, we first study the dependence of the gap and effective mass on the carrier concentration ρ. We then investigate the robustness of magnetism by studying the dependencies of the exchange couplings and magneto crystalline anisotropy energy (MAE) on ρ. In agreement with experimental results, we find that magnetism displays a bipolar electrically-tunable character, which is, however, much more robust for hole ($\rho > 0$) rather than electron ($\rho < 0$) doping. Indeed, the MAE vanishes for an electron density $\rho \approx -7.5 \times 10^{13}$ e $\times$ cm^{-2}, signaling the failure of a localized description based on a Heisenberg-type anisotropic spin Hamiltonian. This is in agreement with the rapid increase of the coupling between fourth-neighbor atoms with increasing electron density.

I. INTRODUCTION

The family of atomically thin "beyond graphene" materials is now very large [1,2] and contains also magnetic crystals [3–10], including Cr$_2$Ge$_2$Te$_6$ [11–13], CrI$_3$ [14–27], Fe$_3$GeTe$_2$ [28,29], CrBr$_3$ [30,31], and CrCl$_3$ [32]. Given their two-dimensional (2D) nature, these materials are being actively investigated as building blocks in van der Waals (vdW) heterostructures to fabricate novel spintronic devices with ultra-small footprint [33–35]. In addition, their 2D nature paves the way for achieving an unprecedented control of magnetism via the electrical field effect.

Though most of these magnets behave as 2D semiconductors, very few groups [12,17,19,36–39] have been able to fabricate devices displaying field-effect-transistor-type behavior. Experimental work [19] on monolayer CrI$_3$, for example, revealed that the magnetic properties of this material can be modulated electrically. In fact, hole (electron) doping strengthens (weakens) the magnetic order. Furthermore, an electron doping $\rho \sim -2.5 \times 10^{13}$ e $\times$ cm^{-2} in bilayer CrI$_3$ induces a transition from an antiferromagnetic to a ferromagnetic ground state. This magnetic switching seems to be fully dominated by electrostatic effects and the antiferro-to-ferro phase transition appears to be facilitated by the formation of magnetic polarons [40]. Similarly, Zhang *et al.* [36] were able to tune the antiferromagnetic resonances of bilayer CrI$_3$

by carrier doping, confirming that electrostatic gating is a powerful tool to modulate various magnetic properties.

Electrostatic gating has also employed to modulate the magnetic properties of Cr$_2$Ge$_2$Te$_6$. Few-layer Cr$_2$Ge$_2$Te$_6$ exhibits bipolar gate tunability, although much stronger effects have been observed for electron-type doping [12,37,38]. As expected, the *I-V* characteristics of the fabricated field-effect transistors (FETs) indicate a stronger tunability with decreasing the device thickness. In the window of doping $\rho \in [-7, +7] \times 10^{12}$ e $\times$ cm^{-2}, the Curie critical temperature $T_{\rm C}$ is almost constant, $T_{\rm C} \sim 55$ K [12], while for a heavy electron doping of $\rho \sim -4 \times 10^{14}$ e $\times$ cm^{-2} a large enhancement of $T_{\rm C}$—up to $T_{\rm C} \sim 200$ K—is observed. Heavy electron doping can also switch the sign of the magnetic anisotropy energy (MAE), leading to a change in the magnetic easy axis, from out-of-plane to in-plane. Verzhbitskiy *et al.* [37] observed that, at high electron densities, the sheet resistance of few-layer Cr$_2$Ge$_2$Te$_6$ decreases with increasing temperature, indicating a metallic character. From Hall effect measurements, they inferred the occurrence of an insulator-to-metal transition at $\rho \sim -4 \times 10^{14}$ e $\times$ cm^{-2}.

On purely theoretical grounds, we conclude by stating that doping a 2D magnetic insulator opens also a wealth of intriguing possibilities in the realm of 2D plasmonics [41]. Indeed, it has been demonstrated that spin waves couple to the charge collective modes (i.e., plasmons) of the itinerant electron system [42]. These plasmon-magnon interactions naturally arise from the exchange interaction between the itinerant carriers and the localized magnetic moments hosted by the lattice and do not require spin-orbit coupling to exist. Other

*guido.menichetti@df.unipi.it

mechanisms explaining the origin of plasmon-magnon coupling in 2D magnetic crystals have been proposed in the recent literature. In the case of a topological insulator (TI), Efimkin and Kargarian [43] proposed that the helical nature of spin-momentum locking of Dirac-type surface states is responsible for magnon-plasmon coupling (for earlier work on coupling between charge and spin modes on the surface of a TI see also Ref. [44]). Costa *et al.* [45] and Dyrda *et al.* [46] showed that plasmon-magnon coupling can arise from the interaction between the electromagnetic field of plasmon oscillations and localized spins in a magnet via the direct Zeeman coupling and inverse spin galvanic effect, respectively. The presence of itinerant charge carriers induced via the electrical field effect is the common ingredient in all these works [42–46] on plasmon-magnon interactions.

Despite this body of literature, we are unaware of theoretical investigations of the doping dependence of the magnetic properties of 2D vdW materials. There are two ways of studying such dependence. One procedure, dubbed as "rigid doping," assumes that the 2D material under study is uniformly doped and overall charge neutrality is compensated through a jellium background. This approach is plagued by an intrinsic problem: no external electric field, which can be greater than ≈ 1.5 Volt/Å, is included in the corresponding calculations. As a result, the induced charge density distributes uniformly throughout the simulation cell, even in the vacuum region far from the 2D material and, in the case of thicker flakes, in the bulk of the sample.

The second approach [47–50], which is used in this article, relies on an effective parallel-plate capacitor model in which one of the plates is a charged layer (here labeled metal gate) and the other "plate" is the 2D material of interest—see Fig. 1(a). Given the atomic-scale distance between the gate and the 2D material in Fig. 1(a), this second approach loyally mimics the physisorbed electrical double layer that forms in real devices where ionic liquids are used to achieve large carrier densities such as those ($|\rho| \sim 10^{14}$ e $\times$ cm^{-2}) explored in this article. In this second approach, one is able to reproduce the strongly localized voltage drop at the surface of the 2D material and the consequent charging.

In this article, we present an *ab initio*, density functional theory (DFT) [51,52] study of the doping dependence of the electronic, structural, and magnetic properties of monolayer $Cr_2Ge_2Te_6$, which is a prototypical 2D magnetic semiconductor. In order to this end, we do not assume "rigid doping" but, rather, employ the field effect configuration depicted in Fig. 1(a). We use a *hybrid* functional to properly take into account the role of nonlocal electron-electron interaction effects [53–57]. As discussed at length in our previous work [53], such functional transcends the severe limitations that the commonly used LDA + U/GGA + U approaches [58–60] have displayed in the context of 2D magnetism. In passing, we note that the experimental works [12,37] on $Cr_2Ge_2Te_6$ cited above contain results of DFT calculations. These, however, concentrated only the role of "rigid doping" on bulk $Cr_2Ge_2Te_6$ and were carried out using the LDA + U/GGA + U approaches, which neglect the crucial role of nonlocal electron-electron interactions.

This article is organized as following. In Sec. II we present a brief discussion of our theoretical method (Sec. II A)
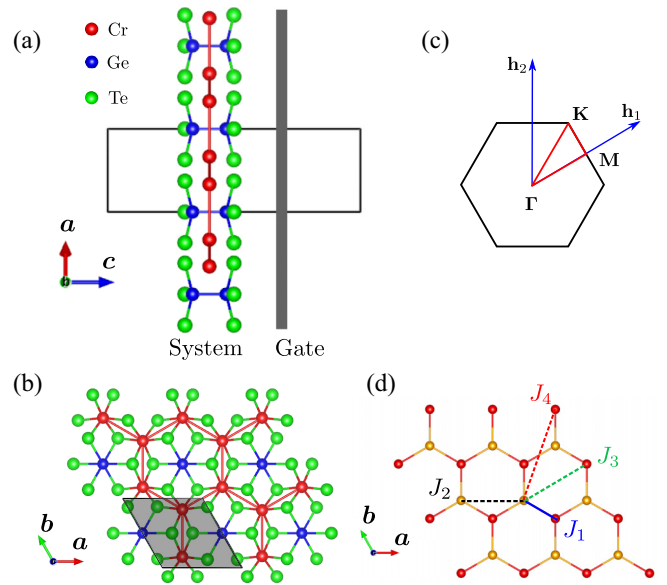

FIG. 1. (a) Monolayer $Cr_2Ge_2Te_6$ placed in front of a metal gate. When a uniform charged plane is placed in front of the system, the latter is charged with the same amount of opposite charge. (b) Top view of monolayer $Cr_2Ge_2Te_6$. In grey, the rhombohedral unit cell. (c) The corresponding Brillouin zone with the high-symmetry points used for the calculation of the electronic band structure [52]. d) Intralayer exchange couplings between Cr atoms (orange and red refer to nonequivalent atoms): J_1, J_2, J_3, and J_4 denote the coupling between nearest-neighbor, second-neighbor, third-neighbor, and fourth-neighbor atoms, respectively.

and a description of the device geometry (Sec. II B). In Sec. III we present a summary of our main numerical results on the electronic structure of monolayer $Cr_2Ge_2Te_6$ in the presence of an electrostatic gate. Results on the doping dependence of the exchange couplings and MAE are instead reported in Sec. IV. A summary of our main findings and a brief set of conclusions are finally presented in Sec. V. A wealth of additional numerical results is reported in the Appendix.

II. THEORETICAL APPROACH

In this section, we first discuss the computational tools we have used (Sec. II A) and then (Sec. II B) present the details of the device geometry (crystal structure of monolayer $Cr_2Ge_2Te_6$ and FET geometry). Uninterested readers can skip Sec. II A and jump directly to Sec. II B.

A. Computational details

We perform DFT calculations by using the QUANTUM ESPRESSO (QE) [61–63] and CRYSTAL17 [64,65] codes, which use plane waves and atom-centered (Gaussian) basis sets, respectively.

For the calculations with QE we use the SG15 optimized norm-conserving Vanderbilt (ONCV) pseudopotentials [66–68], including also the contribution from spin-orbit coupling (SOC). We use an energy cutoff up to 70 Ryd
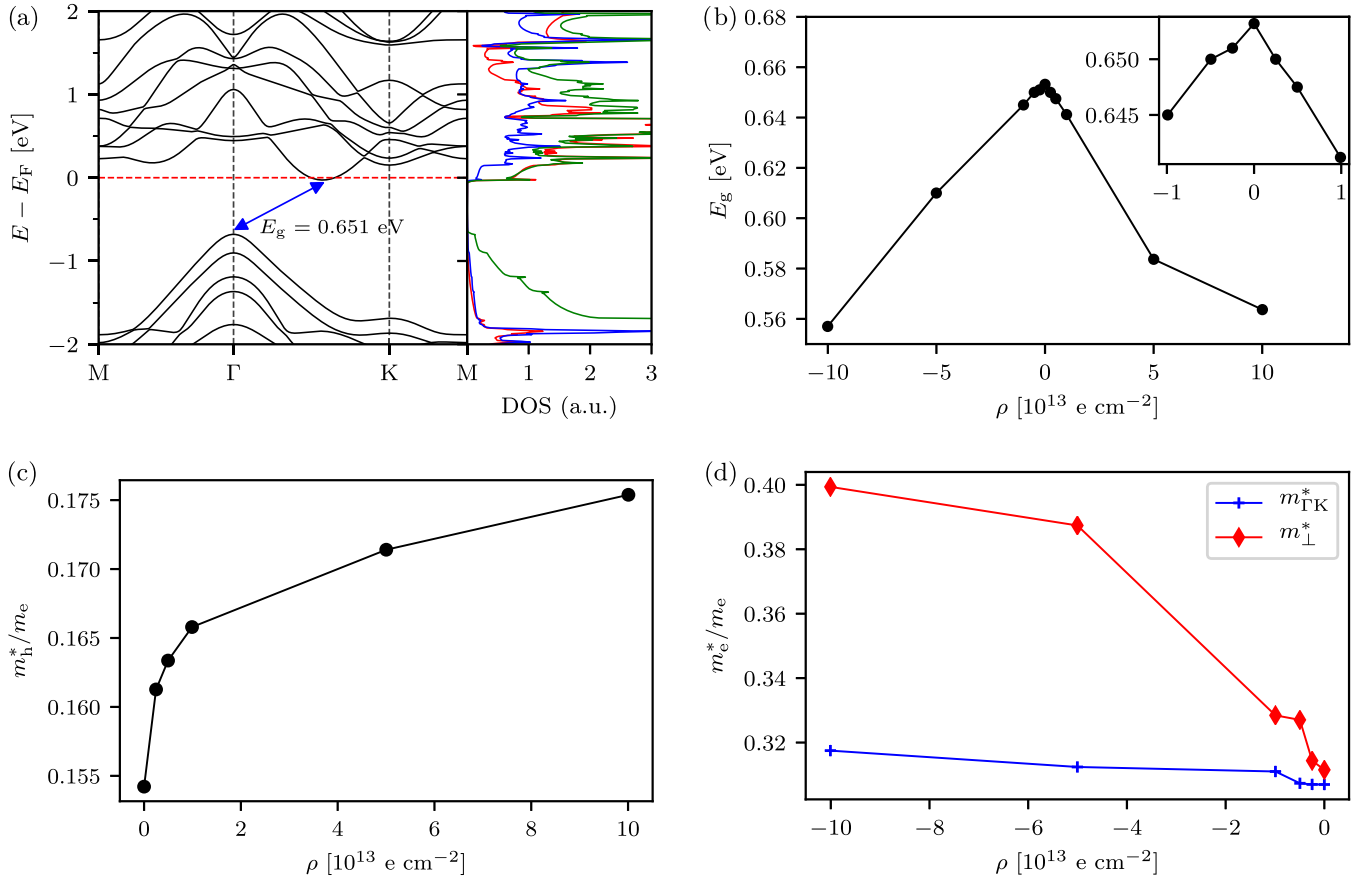
FIG. 2. Panel (a) Relativistic band structure and projected density of states (DOS) of monolayer $Cr_2Ge_2Te_6$ in the ferromagnetic state. Data in this panel refer to an electron charge density $\rho = -2.5 \times 10^{12}\,\mathrm{e\,cm^{-2}}$ (corresponding to -0.01 e/cell) and have been obtained with the HSE06 hybrid functional. In the DOS panel, colors refer to the DOS as projected onto the atomic orbitals of the various atoms (as in Fig. 1): Cr-$3d$ (red), Ge-$4p$ (blue), and Te-$5p$ (green). The HSE06 hybrid functional yields an insulating ferromagnetic state with an indirect gap $E_g \sim 0.651\,\mathrm{eV}$. (b) Dependence of the indirect electronic gap E_g on the doping charge ρ. In the inset a zoom of the results relative to the interval $\rho \in [-1, 1] \times 10^{13}\,\mathrm{e\,cm^{-2}}$ is shown. (c) Dependence of the effective mass (in unit of the bare electron mass in vacuum m_e) for holes (m_h^*) as a function of ρ. (d) Same as in panel (c) but for electrons: $m_{\Gamma K}^*$ ($m_\perp^*$) refers to the electron effective mass evaluated at the minimum of the conduction band along the direction ΓK (orthogonal to ΓK) of the BZ. In panels (b–d), filled symbols represent the calculated points while solid lines are just guides to the eye.

for all the calculations. We adopt the HSE06 [69], hybrid exchange-correlation (xc) functional, which mixes the Perdew-Burke-Ernzerhof (PBE) exchange [70] with 25% of the exact nonlocal Hartree-Fock exchange, thereby including nonlocal electron-electron interaction effects [53]. The vdW-D2 correction is included through the method proposed by Grimme [71]. For the Brillouin zone (BZ) integration we employ a Marzari-Vanderbilt smearing [72] of 10^{-3} Ryd with a Monkhorst-Pack (MP) [73] $\boldsymbol{k}$-point grid with $8 \times 8 \times 1$ for self-consistent calculations of the charge density.

For the calculations with CRYSTAL17 we use a 86-411d41 Gaussian all-electron basis set [74] with 24 valence electrons for Cr and a double-zeta basis set with an effective core pseudo-potential (m-cc-pVDZ-PP) [75] with 24 valence electrons for Te and 22 valence electrons for Ge. The charge density integration over the BZ are performed using a uniform 24×24 MP $\boldsymbol{k}$-point grid. When we use a super-cell, we scale the MP grid size to assure the same accuracy as in the single-cell calculations.

In order to evaluate fully relativistic electronic band structures with the HSE06 hybrid xc functional, we used the WANNIER90 [76] code. In fact, at odd with the case of semilocal functionals depending only on the density or the density and its gradient, band structure calculations in the case of hybrid functionals require the knowledge of the electronic wave functions in all points where the bands need to be calculated. However, at the end of the self-consistent run, the wave functions are known only on a uniform grid in the BZ. Thus, an interpolation scheme is needed to extract the electronic structure along high symmetry directions.

The WANNIER90 code allows us to overcome this problem interpolating the electronic band structure using Maximally Localized Wannier Functions (MLWFs) [77,78] extracted from the DFT calculations with QE. As starting guess for the "Wannierization" procedure, we project the Bloch states onto trial localized atomiclike orbitals: d orbitals for the Cr atoms, p orbitals for Te atoms, and p_z orbital for Ge atoms. We made this choice analyzing the composition of the density of states around the Fermi energy, as shown in Fig. 2(a).

We use CRYSTAL17 to evaluate the exchange coupling parameters to reduce the computational cost due to the size of the super-cell and therefore the high number of atoms. In particular, we evaluate the magnetic exchange couplings, with the HSE06 hybrid functional, in a 4×4 super-cell with 160 atoms. We have been able to switch from QE to CRYSTAL17 after testing the consistency of the results with both codes, comparing electronic band structures, relaxed atomic positions, and charge distribution in the FET setup.

Finally, we use the VESTA [79] and XCRYSDEN [80] codes to visualize the geometrical structure and BZs—see Fig. 1.

B. Geometrical structure and FET Setup

Bulk $Cr_2Ge_2Te_6$ forms a layered structure with monolayers separated by a vdW gap [53]. Each monolayer—Figs. 1(a) and 1(b)—is formed by edge-sharing $CrTe_6$ octahedra where the Ge pairs are located in the hollow sites formed by the octahedra honeycomb. In Fig. 1(a) we present the FET device geometry we have studied. It consists of monolayer $Cr_2Ge_2Te_6$ placed in front of a metal gate, which is modeled as a uniformly charged plane with a charge density $-\rho$. The charged plane was placed at a distance $d_g = 4.5$ Å from the $Cr_2Ge_2Te_6$ layer. Spurious interactions between the fundamental unit represented by monolayer $Cr_2Ge_2Te_6$ placed in front of the gate and its periodic replicas (due to the fact that we do calculations by imposing periodic boundary conditions in all directions) must be accounted for carefully as discussed at length in Ref. [47]. Finally, a potential barrier of height $V_b = 10$ Ryd and width $d_b = 2$ Å was used to simulate the gate dielectric and to prevent ions from moving too close to the gate. (We have checked that the final results were independent of the barrier height and width, provided that one explores a range of values of V_b and d_b such that electrons do not spill towards the gate for large electron doping.) The internal, three-layer structure of monolayer $Cr_2Ge_2Te_6$ therefore acquires the same amount of opposite charge, yielding a finite electric field in the region between the "system" and the gate [47–50]—see Appendix A. Finally, in Fig. 1(c) we illustrate the BZ of monolayer $Cr_2Ge_2Te_6$.

For the calculation of the electronic and magnetic properties of monolayer $Cr_2Ge_2Te_6$ we use the hexagonal unit cell shown in Fig. 1(b). We consider a super-cell with about 15 Å of vacuum along the $\hat{z}$ direction between periodic images. We have decided to adopt the experimental lattice parameters to compare on equal footing the results obtained via QE with those obtained via CRYSTAL17 [53]. Using the experimental lattice constants [81,82] $a = b = 6.8275$ Å, we relaxed the atomic positions until the maximum force on all atoms was less than 10^{-4} Ryd/Bohr. Relaxation of the atomic positions has been carried out in the ferromagnetic phase using using the PBE xc functional. We repeat such procedure for each doping ρ, although we have not observed significant structural variations with changes in this parameter.

Throughout this article, ρ, measured in units of e $\times$ cm^{-2}, denotes the doping charge density, where e $= |-e| > 0$ is the magnitude of the elementary charge $-e$. This means that $\rho < 0$ ($\rho > 0$) denotes electron (hole) doping. We explore the following range of doping: $\rho \in [-1, +1] \times 10^{14}$ e $\times$ cm^{-2}.

III. ELECTRONIC STRUCTURE

In this section we present our main results for the electronic structure of monolayer $Cr_2Ge_2Te_6$ in the FET device geometry.

In Fig. 2(a) we show the relativistic electronic band structure of monolayer $Cr_2Ge_2Te_6$ in the ferromagnetic state, with an electron doping of $\rho = -2.5 \times 10^{12}$ e cm^{-2} (-0.01 e/cell). We find an almost rigid translation of the band profile as compared to the undoped case [53]. This is in stark contrast with the case of transition-metal dichalcogenides [48], where significant differences between "rigid doping" and field effect calculations have been reported.

The density of states (DOS), projected onto the atomic orbitals, is also reported in Fig. 2(a). Our results for the DOS demonstrate that the main contribution to the electronic bands near the Fermi energy comes from the $Cr - 3d$ and $Te - 5p$ orbitals, which are strongly hybridized [53]. Such hybridization is very weakly affected by the doping charges. We remind the reader that the Te atoms have a fundamental role in stabilizing the ferromagnetic phase of $Cr_2Ge_2Te_6$ because they mediate super-exchange interactions in the Cr-Te-Cr bonds, as per the Goodenough-Kanamori rule [83,84]. This was also confirmed in a recent angle-resolved photoemission spectroscopy study on bulk $Cr_2Ge_2Te_6$ [85].

As we will see below in Sec. IV—and in agreement with experimental results on few-layer $Cr_2Ge_2Te_6$ [12,37]—the magnetic properties of monolayer $Cr_2Ge_2Te_6$ change in a much stronger fashion for electron-type (rather than hole-type) doping. Indeed, the magnetic moment localized on the Cr atom increases linearly with the doping charge for both dopings, but the rate of change is much lower for hole-type doping—see Fig. 7 in the Appendix. This behavior can be explained by looking again at the DOS in Fig. 2(a): by adding electrons to the system, states of the Cr atom are immediately populated thereby yielding an increase of the its magnetic moment. On the contrary, a hole-type doping influences mainly the Te $5p$ orbitals, leading to a much weaker effect on the Cr magnetic moment (and, in turn, to a much weaker tunability of magnetism for holes).

In Fig. 2(b) we plot the dependence of the magnitude of the (indirect) electronic band gap E_g on doping ρ. We clearly see an approximately *linear* decrease of E_g with increasing ρ, with E_g decreasing of about 10 meV from its undoped ($\rho = 0$) value ($E_g|_{\rho=0} \sim 0.66$ eV) to its value at $\rho \pm 10^{14}$ e $\times$ cm^{-2} (i.e., $E_g \sim 0.56$ eV).

Due to our interest in the q dispersion of plasmon modes of doped 2D vdW magnets (and their coupling to spin waves) [42], we also evaluated the effective mass of holes (electrons) via a parabolic fitting of the top (bottom) of the valence (conduction) band. While the hole effective mass m_h^* is isotropic near the Fermi level, the electron effective mass m_e^* is not. In fact, the Fermi surface near the bottom of the first conduction band has an ellipsoidal shape with the short axis along the ΓK direction of the BZ. We therefore decompose the electron effective mass m_e^* in two components: $m_{\Gamma K}^*$ and $m_\perp^*$, which are evaluated by fitting the minimum of the conduction band along the ΓK direction and the direction orthogonal to it, respectively. In Fig. 2(c) [Fig. 2(d)] we report our results for
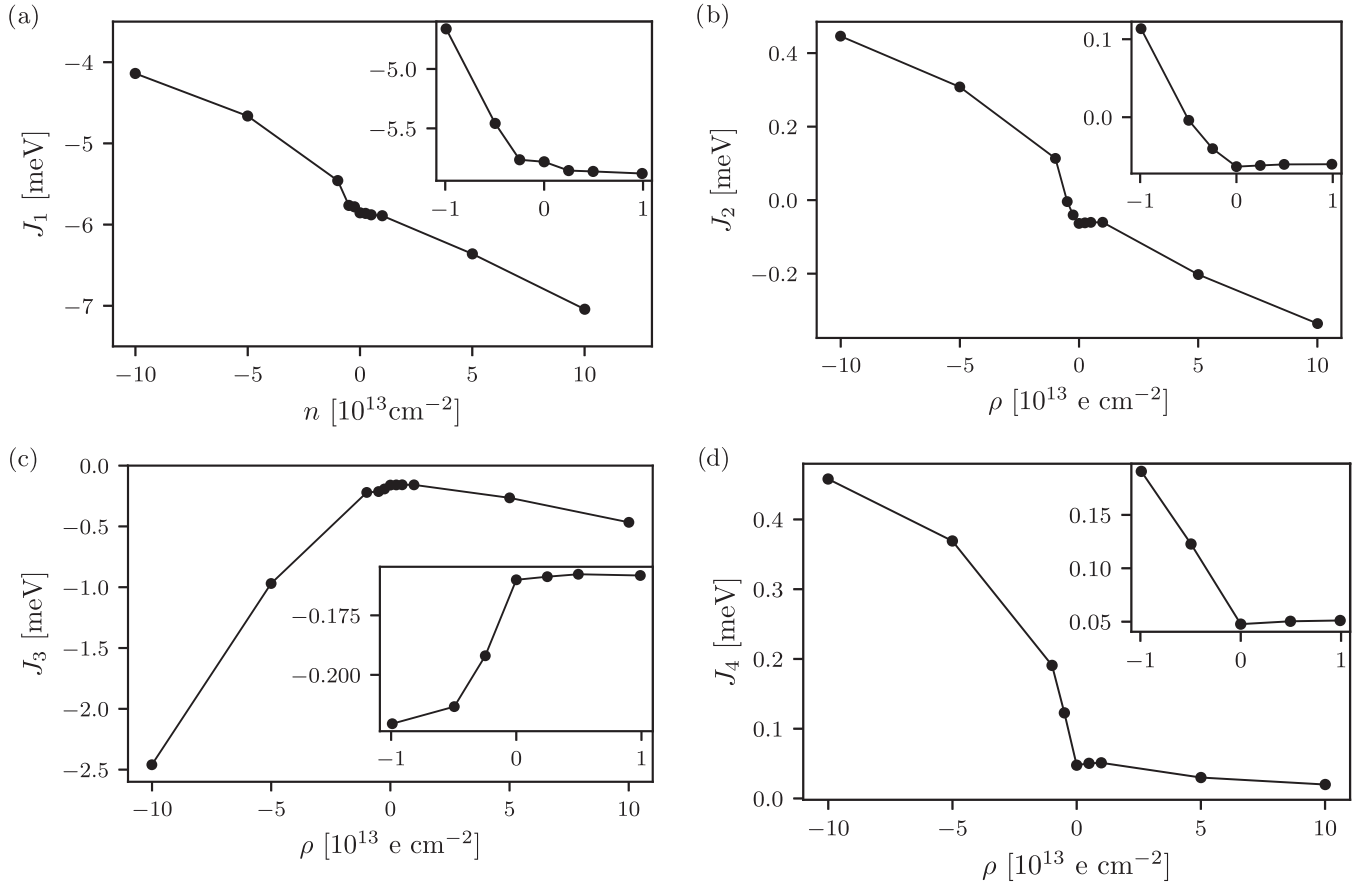
FIG. 3. Intralayer exchange coupling parameters J_i—defined in Fig. 1—as functions of the doping charge ρ. The inset in every panel shows a zoom of the results relative to the interval $\rho \in [-1, +1] \times 10^{13}$ e cm^{-2}. In all panels, filled circles are the calculated data points while solid lines are just guides to the eye.

m_{h}^{*} (m_{e}^{*}). Electrostatic doping increases m_{h}^{*} and $m_{\perp}^{*}$, while $m_{\Gamma K}^{*}$ remains approximately constant.

IV. EXCHANGE COUPLINGS AND MAGNETO CRYSTALLINE ANISOTROPY

We now turn to discuss about the dependence on ρ of the magnetic properties of monolayer Cr$_2$Ge$_2$Te$_6$.

In order to understand the microscopic properties of magnetic materials it is crucial to map the *ab initio* results onto an effective spin model. In the case of localized magnetic moments, the Heisenberg spin Hamiltonian can be used [86,87]. In our previous work [53], we calculated all the relevant exchange couplings (and the MAE) for monolayer, bilayer, and bulk Cr$_2$Ge$_2$Te$_6$, with the HSE06 hybrid functional. Here, we greatly extend this previous study by calculating how the intralayer exchange couplings of monolayer Cr$_2$Ge$_2$Te$_6$ change with ρ. On the one hand, these calculations allow us to understand the range of values of ρ where a localized description of magnetism based on the Heisenberg spin Hamiltonian is valid. On the other hand, our results allow us to understand the mechanism that enables electrical control of magnetism. Indeed, a high level of doping may affect the super-exchange mechanism that stabilizes the ferromagnetic ground state.

The spin Hamiltonian we use has the following form (see Ref. [53] and references therein to earlier work):

$$\hat{\mathcal{H}}_{\mathrm{spin}} = \sum_{i<j} J_{ij}\hat{\boldsymbol{S}}_i \cdot \hat{\boldsymbol{S}}_j + \sum_i A_i \hat{S}_{iz}^2. \qquad (1)$$

(i) The first term on the right-hand side of Eq. (1) is the rotationally invariant Heisenberg Hamiltonian with exchange couplings J_{ij}, the sum over i, j running over all the Cr pairs without double counting.

(ii) The second term is the MAE, the sum over i running over all the Cr sites. (We remind the reader that this term is crucial to stabilize long-range magnetic order in 2D [88,89] since it lifts the rotational invariance of the first term in Eq. (1), effectively allowing to bypass the Mermin-Wagner theorem [88].) The MAE, which stems from SOC [90,91], can be calculated [11,53,91,92] by looking at the total energy difference—obtained through self-consistent calculations in the presence of SOC—between the configuration with all spins aligned along the $\hat{z}$ direction (i.e., perpendicular to the plane hosting monolayer Cr$_2$Ge$_2$Te$_6$) and that with all spins aligned along the $\hat{x}$ or $\hat{y}$ direction (i.e., parallel to the plane hosting monolayer Cr$_2$Ge$_2$Te$_6$). A positive (negative) sign of the MAE means that the system is an easy-plane (easy-axis) ferromagnet.

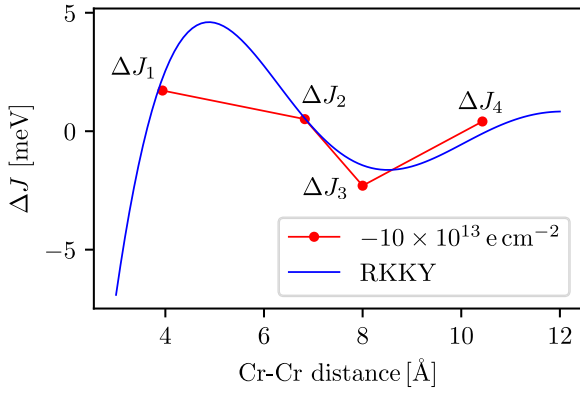(iii) We emphasize that Eq. (1) does not contain a Dzyaloshinski-Moriya (DM) interaction term of the form

FIG. 4. The difference ΔJ (filled red circles) between the exchange couplings evaluated at finite ρ and the same quantities evaluated for $\rho = 0$ (i.e., in the undoped system). On the horizontal axis we have displayed the Cr − Cr distance. Results in this plot refer to $\rho = -10^{14}$ e cm^{-2}. The oscillating behavior of ΔJ is fitted (blue curve) with an RKKY interaction for a 2D electron gas model [51,102,104].
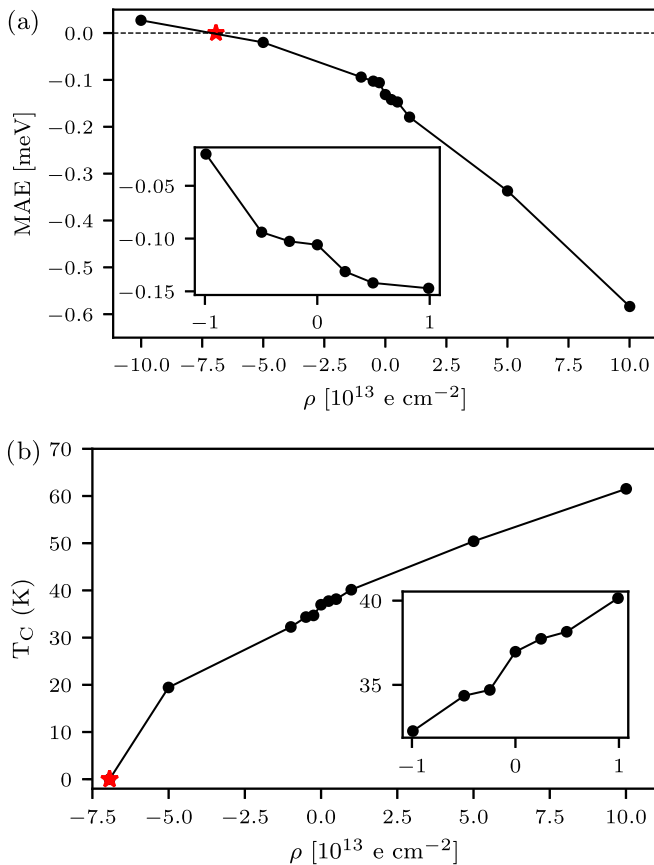

FIG. 5. Panel (a) MAE (per Cr atom) as a function of the doping charge ρ. The red star denotes the value of electron doping ρ_c at which the MAE vanishes (i.e., $\rho_c \approx -6.4 \times 10^{13}$ e cm^{-2}). At this value of doping the Curie temperature T_C vanishes. Panel (b) Curie temperature T_C as a function of doping charge ρ. In the inset we report a zoom of the results relative to the interval $\rho \in [-1, 1] \times 10^{13}$ e cm^{-2}. In both panels, filled circles are the calculated points—according to Eqs. (2) and (3)—while solid lines are just guides to the eye.

$\sum_{i<j} \boldsymbol{D}_{ij} \cdot (\hat{\boldsymbol{S}}_i \times \hat{\boldsymbol{S}}_j)$. This is certainly fully justified in the case of a free-standing monolayer Cr$_2$Ge$_2$Te$_6$ due to the presence of an inversion symmetry center [93]. However, the presence of an electric field orthogonal to the atomically thin system breaks such symmetry and a nonzero DM should be, at least in principle, taken into account [94]. However, we do expect such contribution to be very small in magnitude, on the order of $\sim\mu$eV, as reported in Ref. [94] for the case of CrI$_3$, because, as discussed in Sec. III, the electrical field effect geometry in the present case induces an almost rigid shift of the band structure and no significant structural changes.

Microscopic calculations of the exchange couplings J_{ij} are more subtle than the MAE. As discussed at length in Ref. [53], an accurate method to calculate J_{ij} for small-gap semiconductors and metals is the four-state mapping analysis (FSMA) approach [95–98]. The FSMA approach considers one specific magnetic pair at a time in a super-cell. Such method is accurate when the super-cell used for the calculations is large enough. In fact, we can monitor the accuracy of the calculated exchange coupling by increasing the super-cell size [53]. In the present case of a doped system, we observed that we need at least a 3×3 super-cell of monolayer Cr$_2$Ge$_2$Te$_6$ to have converged results with doping charge in the range $\rho \in [-1, +1] \times 10^{13}$ e cm^{-2}. For values of ρ outside this interval we were forced to use a $\sqrt{13} \times \sqrt{13}$ super-cell—see Figs. 8 and 9 in the Appendix.

A. Exchange couplings

In Fig. 3 we present our results for the intralayer exchange couplings $J_1, \ldots, J_4$ (defined in Fig. 1), which are plotted as functions of the doping charge ρ. These results have been calculated with the HSE06 hybrid functional, but without the inclusion of SOC. The reason is that we do not expect that SOC contributes appreciably to the exchange couplings as the magnetic moments of the Cr atoms do not chance significantly with the inclusion of SOC [53]. For $\rho \in [-1, +1] \times 10^{13}$ e cm^{-2}, we observe much stronger effects for electron-type doping. For this type of doping, indeed, all the exchange couplings J_i display an almost linear dependence on $\rho < 0$: see the insets in Figs. 3(a)–3(d). For hole-type doping J_i are roughly independent of ρ. These results are in agreement with the DOS analysis discussed earlier in Sec. III and the experimental results reported in Ref. [12].

The situation becomes more complicated for larger values of ρ: see main panels in Figs. 3(a)–3(d). Increasing $\rho < 0$ to values larger than -10^{13} e cm^{-2}, J_1 is significantly reduced, reaching $J_1 \approx -4$ meV for $\rho = -1 \times 10^{14}$ e cm^{-2}. In the same interval, J_2 changes sign, while remaining much smaller than J_1 in magnitude, thereby not altering the ferromagnetic order. For large values of $\rho < 0$, J_3 becomes large and negative (thereby contributing to the stabilization of ferromagnetism), reaching $J_3 \approx -2$ meV for $\rho = -1 \times 10^{14}$ e cm^{-2}. Such a large value of J_3 suggests a change in character of magnetism, from a strongly localized to a rather delocalized type, for heavy electron doping. This is the reason why we evaluated also the fourth-neighbor exchange coupling J_4 [99]. This coupling is on the order of 0.01 meV in the undoped system (and for small values of ρ) but it becomes significantly
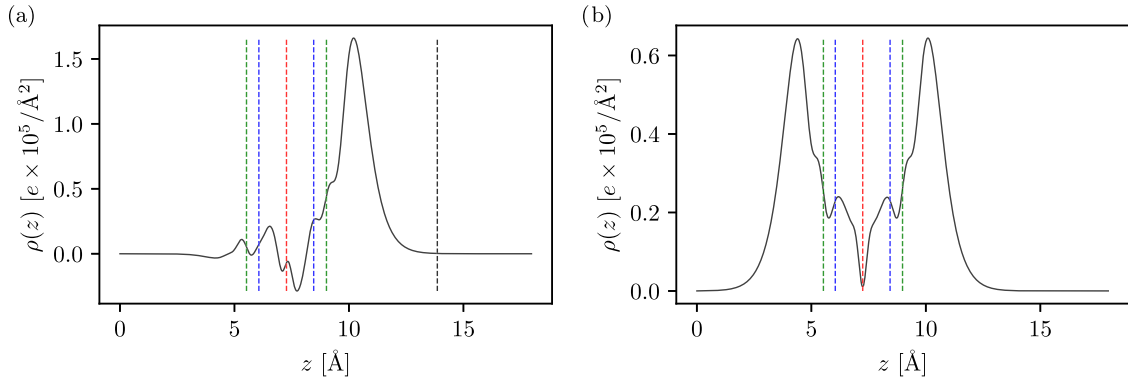
FIG. 6. Doping density $\rho(z)$ of monolayer $Cr_2Ge_2Te_6$ as a function of z. The vertical dashed lines indicate the position of the atoms, the color coding being identical to that reported in Fig. 1(a) of the main text. In panel (a) we clearly see that the doping charge mainly accumulates in the inner layers of $Cr_2Ge_2Te_6$ closer to the gate. In panel (b) we plot the same quantity as in panel (a) but for the case of "rigid doping."

large for large values of $\rho < 0$. We find $J_4 \approx -0.6$ meV for $\rho = -10^{14}$ e cm^{-2}.

These trends of the exchange couplings suggest that, for large values of $\rho < 0$, a long-range, carrier-mediated interaction emerges (on top of the local, super-exchange mechanism). Examples include interactions mediated by the double-exchange mechanism [37,100] or Ruderman-Kittel-Kasuya-Yosida (RKKY) interactions [51,52,101,102]. These phenomena arise due to the delocalized nature of the conduction bands, which stems from the hybridization of the $Cr - 3d$ orbitals with the $Te - 5p$ orbitals [53]. In Fig. 4 we plot the difference ΔJ between the exchange couplings in the presence and absence of doping charge, as a function of the $Cr - Cr$ bond length. An RKKY model for 2D systems [51,101–105] fits well our numerical data. Such qualitative validity of the RKKY fit corroborates the metallic character of magnetism observed experimentally [37] for large values of $\rho < 0$. From a theoretical point of view, much more work is however needed to precisely establish which long-range scenario better describes the magnetic properties of monolayer $Cr_2Ge_2Te_6$ for large values of $\rho < 0$.

The dependence of the exchange couplings on ρ for holes ($\rho > 0$) is not as complicated as for electrons. As clear in
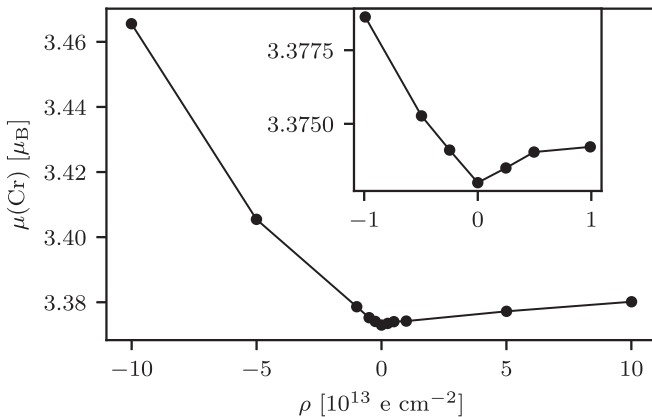

FIG. 7. Calculated magnetic moment of Cr (in units of the Bohr's magneton μ_B) as a function of the doping charge ρ. In the inset we report a zoom of the results relative to the interval $\rho \in [-1, 1] \times 10^{13}$ e cm^{-2}.

Fig. 3, after a small plateau for small values of $\rho > 0$, the exchange couplings increase with increasing $\rho > 0$, leading to a more stable ferromagnetic order. The largest changes with $\rho > 0$ are observed in J_1 and J_2, while J_3 and J_4 do not change significantly, even for large values of $\rho > 0$. This suggests that, contrary to what discussed above for electrons, magnetic order retains its localized character with increasing $\rho > 0$, even at high hole densities—see Figs. 10 and 11 in the Appendix to see the stability of ferromagnetic phase in monolayer $Cr_2Ge_2Te_6$ with respect to changes in ρ and results for the exchange couplings obtained in the "rigid doping" approach.

B. Magneto crystalline anisotropy energy

In Fig. 5(a) we presents our results for the dependence of the MAE (per Cr atom) on ρ. We clearly see that the MAE increases in absolute value for hole-type doping ($\rho > 0$). Once again, the situation for electron-type doping is dramatically different. With increasing $\rho < 0$, the MAE first decreases and then changes sign at $\rho_c \sim -6.4 \times 10^{13}$ cm^{-2}. (This critical value ρ_c has been obtained by interpolating in a linear fashion between two results for the MAE, one obtained at $\rho = -10^{14}$ e cm^{-2} and one at $\rho = -5 \times 10^{13}$ e cm^{-2}.) This signals a change in the magnetic easy axis, from out-of-plane to in-plane. At this value of electron doping, long-range magnetic order ceases to exist due to the Mermin-Wagner theorem [88]. We also estimate the Curie temperature T_C by considering only the largest exchange coupling (i.e., J_1) and the MAE. We use an expression for T_C proposed by the authors of Ref. [89], which reads as follows:

$$T_C = T_C^{Ising} f\left(\frac{A}{J_1}\right), \tag{2}$$

with

$$f(x) = \tanh^{1/4}\left[\frac{6}{N_{nn}} \log(1 + \gamma x)\right]. \tag{3}$$

Here, A coincides with the MAE, N_{nn} is the number of nearest neighbors (3 in our case), $\gamma = 0.033$, and $T_C^{Ising} = 1.52S^2 J_1/k_B$.

Using the calculated dependencies of J_1 and A on ρ inside Eq. (2) we obtain the Curie temperature trend reported in
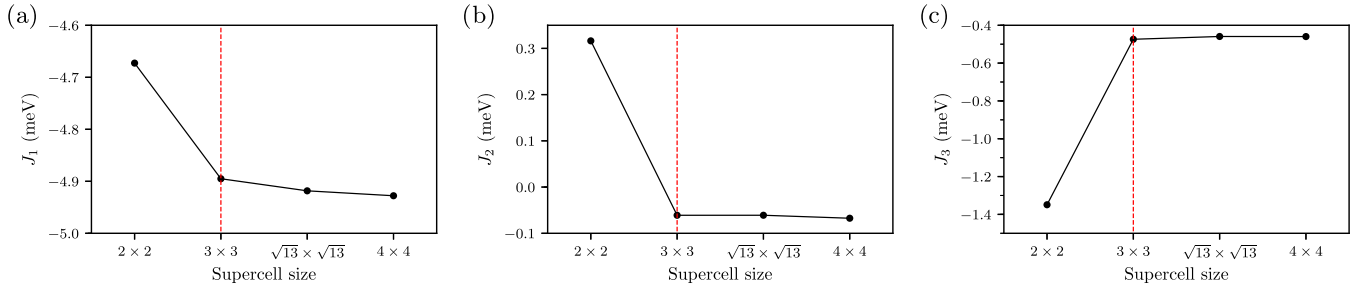
FIG. 8. Convergence of the intralayer exchange coupling parameters J_1, J_2, and J_3 of monolayer $Cr_2Ge_2Te_6$ with the size of the super-cell. Results in this figure refer to a doping $\rho \approx -5 \times 10^{12}$ cm^{-2} and have been obtained in the framework of the PBE functional and in the electrical field effect configuration depicted in Fig. 1(a) of the main text. The red vertical dashed lines denote the values of the super-cell size used in this article.

Fig. 5(b), which is in excellent qualitative agreement with the experimental results of Refs. [12,37] for thin films. Indeed, T_C is almost constant for small doping, i.e., for $\rho \in [-1, +1] \times 10^{13}$ e cm^{-2} while for heavy hole doping T_C is almost twice as large as the critical temperature for the undoped case. A more quantitative analysis between our calculations and the above mentioned experimental results is beyond the scope of the present work for two reasons. On the one hand, we focus on monolayer $Cr_2Ge_2Te_6$ while the results of Refs. [12,37] refer to thin films (T_C has a strong dependence on the thickness of the sample [11,53]). On the other hand, a truly quantitative comparison would require the inclusion of J_2 in a theory of T_C, while Eq. (2) includes only the MAE and J_1.

V. SUMMARY AND CONCLUSIONS

In summary, in this article we have reported on an extensive density functional theory study of the electronic and magnetic properties of the atomically thin magnetic material $Cr_2Ge_2Te_6$, in the presence of an electrical field effect.

Taking into account nonlocal electron-electron interactions through the use of the HSE06 hybrid functional [53], we have
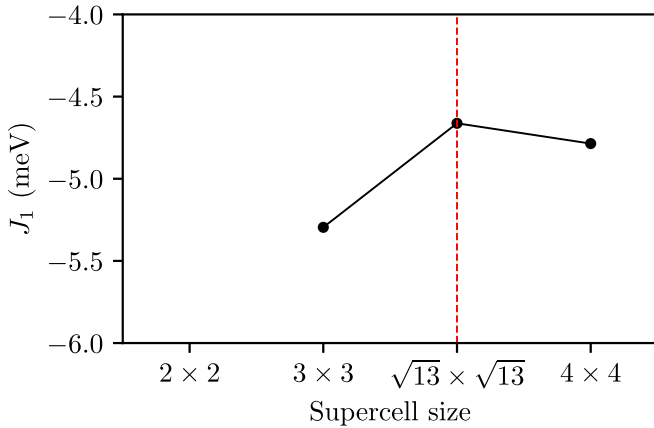

FIG. 9. Convergence of the intralayer exchange coupling parameter J_1 with the size of the super-cell. Results in this figure refer to a doping $\rho \approx -5 \times 10^{13}$ cm^{-2} (i.e., ten times higher than in Fig. 8) and have been obtained in the framework of the HSE06 hybrid xc functional and in the electrical field effect configuration depicted in Fig. 1(a) of the main text. The red vertical dashed line denotes the values of the super-cell size used in this article.

calculated the relativistic electronic band structure of monolayer $Cr_2Ge_2Te_6$ showing its rigidity under the application of an external electric field induced by a nearby metal gate. We have calculated the dependence on the doping charge ρ of the electronic band gap—see Fig. 2(b)—and hole-electron effective masses—see Figs. 2(c) and 2(d). We have then computed the dependence of the magnetic properties on ρ, i.e., the exchange couplings up to the fourth-neighbor one (see Fig. 3), the magneto crystalline anisotropy energy [see Fig. 5(a)], and the approximate Curie temperature T_C [see Fig. 5(b)]. The obtained results have been compared with experimental data, when available.

The nonnegligible values of the fourth-neighbor exchange coupling J_4 at high electron doping signal a change in the character of magnetism and raise questions on the underlaying microscopic mechanism. Qualitatively, our data for heavy electron dopings can be described by an RKKY-type interaction—see Fig. 4. The authors of Ref. [37], however, suggest that, at high doping, a carrier-mediated double-exchange mechanism kicks in. Understanding on theory grounds the best microscopic mechanism responsible for magnetism at high electron dopings is beyond the scope of the present article and is left for future work. More in general, much more experimental work on few-layer $Cr_2Ge_2Te_6$ is needed to assess the microscopic validity of nonlocal functionals for atomically thin 2D materials.

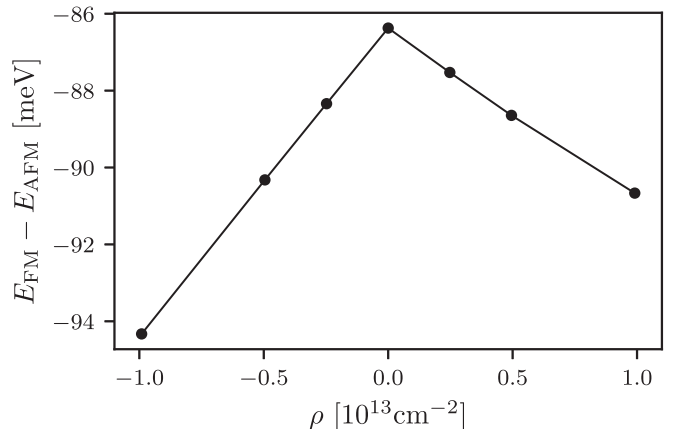FIG. 10. The difference $E_{FM} - E_{AFM}$ between the total energy of the ferromagnetic (E_{FM}) and anti-ferromagnetic (E_{AFM}) phases is plotted as a function of ρ.
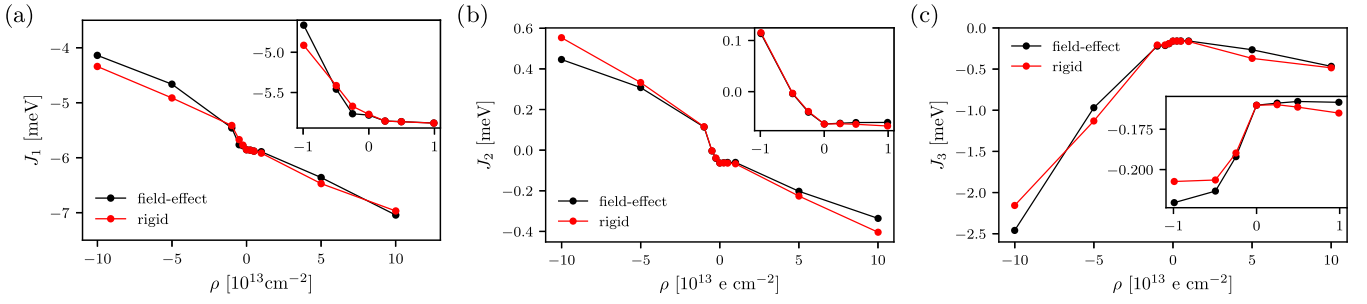
FIG. 11. The three intralayer exchange coupling parameters J_1, J_2, and J_3 are plotted as functions of doping ρ. Results in this plot have been obtained with the HSE06 hybrid functional. The inset in each panel contains results in the interval $\rho \in [-1, 1] \times 10^{13} \, \mathrm{e \, cm^{-2}}$. Results obtained in the simplified "rigid doping" approach (red symbols) are compared to the ones obtained in the electrical field effect approach (black symbols).

APPENDIX: ADDITIONAL NUMERICAL RESULTS

In this Appendix we present additional numerical results.

In Fig. 6(a) we plot the planar averaged doping density $\rho(z)$ due to the presence of the metal gate, after integrating the three-dimensional doping density over the 2D system's area. It has been evaluated as the difference between the full charge density of the doped system and the undoped one. The charge density of the neutral system was calculated with the geometry of the doped one. Corresponding results for the case of rigid doping are reported in Fig. 6(b).

In Fig. 7 we report the calculated magnetic moment of Cr as a function of the doping charge density ρ.

We now briefly summarize the four-state mapping analysis (FSMA) approach [53,95–98]. This approach relies on total-energy calculations but focuses only on the spin configurations of the two ions "linked" by the exchange coupling of interest, leaving all the other ions in the ground-state configuration. Additionally, each magnetic pair is considered individually within a super-cell. The energy expression is

given by

$$E = E_{\mathrm{spin}} + E_0 = J_{12} \boldsymbol{S}_1 \cdot \boldsymbol{S}_2 + \boldsymbol{S}_1 \cdot \boldsymbol{K}_1 + \boldsymbol{S}_2 \cdot \boldsymbol{K}_2 + E_{\mathrm{others}} + E_0, \tag{A1}$$

where E_{spin} and E_0 represent magnetic and nonmagnetic energies, respectively. Here, $J_{12} \boldsymbol{S}_1 \cdot \boldsymbol{S}_2$ is the exchange coupling between sites 1 and 2, and $\boldsymbol{S}_i \cdot \boldsymbol{K}_i$ represents the coupling between site i and all magnetic sites except 1 and 2. Additionally, E_{others} denotes the energy contribution from the interaction between sites 1 and 2 and all other nonmagnetic sites.

Consider the following collinear spin states:

State	$\boldsymbol{S}_1$	$\boldsymbol{S}_2$
1	$(0, 0, S)$	$(0, 0, S)$
2	$(0, 0, S)$	$(0, 0, -S)$
3	$(0, 0, -S)$	$(0, 0, S)$
4	$(0, 0, -S)$	$(0, 0, -S)$

The remaining spin states are held constant according to the ground-state spin configuration. Using Eq. (A1), the energies of the four states are expressed as follows:

$$E_1 = E_0 + J_{12}S^2 + \boldsymbol{S}_1 \cdot \boldsymbol{K}_1 + \boldsymbol{S}_2 \cdot \boldsymbol{K}_2,$$

$$E_2 = E_0 - J_{12}S^2 + \boldsymbol{S}_1 \cdot \boldsymbol{K}_1 - \boldsymbol{S}_2 \cdot \boldsymbol{K}_2,$$

$$E_3 = E_0 - J_{12}S^2 - \boldsymbol{S}_1 \cdot \boldsymbol{K}_1 + \boldsymbol{S}_2 \cdot \boldsymbol{K}_2,$$

$$E_4 = E_0 + J_{12}S^2 + \boldsymbol{S}_1 \cdot \boldsymbol{K}_1 - \boldsymbol{S}_2 \cdot \boldsymbol{K}_2.$$

Solving this system leads to the equality

$$J_{12} = \frac{E_1 - E_2 - E_3 + E_4}{4S^2}, \tag{A2}$$

which represents the FSMA operational definition of the exchange coupling J_{12}. The exchange couplings J_{12} converge as the supercell size increases. In Figs. 8 and 9 we illustrate a summary of our convergence tests in the context of the calculations of the intralayer exchange coupling parameters J_i. All the necessary details are reported in the corresponding figure captions.

In Fig. 10 we present an analysis of the stability of ferromagnetic phase in monolayer $\mathrm{Cr_2Ge_2Te_6}$ with respect to changes in ρ.

In Fig. 11 we compare results for J_1, J_2, and J_3 obtained with two different methods: (i) black symbols denote results obtained in the electrical field effect geometry sketched in Fig. 1(a) of the main text; (ii) red symbols denote results obtained in the "rigid doping" approach.

[1] A. K. Geim and I. V. Grigorieva, Van der Waals heterostructures, Nature (London) **499**, 419 (2013).

[2] N. Mounet, M. Gibertini, P. Schwaller, D. Campi, A. Merkys, A. Marrazzo, T. Sohier, I. E. Castelli, A. Cepellotti, G. Pizzi, and N. Marzari, Two-dimensional materials from high-throughput computational exfoliation of experimentally known compounds, Nat. Nanotech. **13**, 246 (2018).

[3] B. Shabbir, M. Nadeem, Z. Dai, M. S. Fuhrer, Q.-K. Xue, X. Wang, and Q. Bao, Long range intrinsic ferromagnetism in two dimensional materials and dissipationless future technologies, Appl. Phys. Rev. **5**, 041105 (2018).

[4] K. S. Burch, D. Mandrus, and J.-G. Park, Magnetism in two-dimensional van der Waals materials, Nature (London) **563**, 47 (2018).

[5] C. Gong and X. Zhang, Two-dimensional magnetic crystals and emergent heterostructure devices, Science **363**, eaav4450 (2019).

[6] M. Gibertini, M. Koperski, A. F. Morpurgo, and K. S. Novoselov, Magnetic 2D materials and heterostructures, Nat. Nanotechnol. **14**, 408 (2019).

[7] D. Soriano, M. I. Katsnelson, and J. Fernández-Rossier, Magnetic two-dimensional chromium trihalides: A theoretical perspective, Nano Lett. **20**, 6225 (2020).

[8] S. Yang, T. Zhang, and C. Jiang, van der Waals magnets: Material family, detection and modulation of magnetism, and perspective in spintronics, Adv. Sci. **8**, 2002488 (2021).

[9] S. Wei, X. Liao, C. Wang, J. Li, H. Zhang, Y.-J. Zeng, J. Linghu, H. Jin, and Y. Wei, Emerging intrinsic magnetism in two-dimensional materials: Theory and applications, 2D Mater. **8**, 012005 (2021).

[10] Q. H. Wang, A. Bedoya-Pinto, M. Blei, A. H. Dismukes, A. Hamo, S. Jenkins, M. Koperski, Y. Liu, Q.-C. Sun, E. J. Telford, H. H. Kim, M. Augustin, U. Vool, J.-X. Yin, L. H. Li, A. Falin, C. R. Dean, F. Casanova, R. F. L. Evans, M. Chshiev *et al.* The magnetic genome of two-dimensional van der Waals materials, ACS Nano **16**, 6960 (2022).

[11] C. Gong, L. Li, Z. Li, H. Ji, A. Stern, Y. Xia, T. Cao, W. Bao, C. Wang, Y. Wang, Z. Q. Qiu, R. J. Cava, S. G. Louie, J. Xia, and X. Zhang, Discovery of intrinsic ferromagnetism in two-dimensional van der Waals crystals, Nature (London) **546**, 265 (2017).

[12] Z. Wang, T. Zhang, M. Ding, B. Dong, Y. Li, M. Chen, X. Li, J. Huang, H. Wang, X. Zhao, Y. Li, D. Li, C. Jia, L. Sun, H. Guo, Y. Ye, D. Sun, Y. Chen, T. Yang, J. Zhang *et al.* Electric-field control of magnetism in a few-layered van der Waals ferromagnetic semiconductor, Nat. Nanotech. **13**, 554 (2018).

[13] M. Kim, P. Kumaravadivel, J. Birkbeck, W. Kuang, S. G. Xu, D. G. Hopkinson, J. Knolle, P. A. McClarty, A. I. Berdyugin, M. B. Shalom, R. V. Gorbachev, S. J. Haigh, S. Liu, J. H. Edgar, K. S. Novoselov, I. V. Grigorieva, and A. K. Geim, Micromagnetometry of two-dimensional ferromagnets, Nat. Electron. **2**, 457 (2019).

[14] B. Huang, G. Clark, E. Navarro-Moratalla, D. R. Klein, R. Cheng, K. L. Seyler, D. Zhong, E. Schmidgall, M. A. McGuire, D. H. Cobden, W. Yao, D. Xiao, P. Jarillo-Herrero, and X. Xu, Layer-dependent ferromagnetism in a van der Waals crystal down to the monolayer limit, Nature (London) **546**, 270 (2017).

[15] Z. Wang, I. Gutiérrez-Lezama, N. Ubrig, M. Kroner, M. Gibertini, T. Taniguchi, K. Watanabe, A. Imamoğlu, E. Giannini, and A. F. Morpurgo, Very large tunneling magnetoresistance in layered magnetic semiconductor CrI₃, Nat. Commun. **9**, 2516 (2018).

[16] D. R. Klein, D. MacNeill, J. L. Lado, D. Soriano, E. Navarro-Moratalla, K. Watanabe, T. Taniguchi, S. Manni, P. Canfield, J. Fernández-Rossier, and P. Jarillo-Herrero, Probing magnetism in 2D van der Waals crystalline insulators via electron tunneling, Science **360**, 1218 (2018).

[17] B. Huang, G. Clark, D. R. Klein, D. MacNeill, E. Navarro-Moratalla, K. L. Seyler, N. Wilson, M. A. McGuire, D. H. Cobden, D. Xiao, W. Yao, P. Jarillo-Herrero, and X. Xu, Electrical control of 2D magnetism in bilayer CrI₃, Nat. Nanotech. **13**, 544 (2018).

[18] T. Song, X. Cai1, M. W.-Y. Tu, X. Zhang, B. Huang, N. P. Wilson, K. L. Seyler, L. Zhu, T. Taniguchi, K. Watanabe, M. A. McGuire, D. H. Cobden, D. Xiao, W. Yao, and X. Xu, Giant tunneling magnetoresistance in spin-filter van der Waals heterostructures, Science **360**, 1214 (2018).

[19] S. Jiang, L. Li, Z. Wang, K. F. Mak, and J. Shan, Controlling magnetism in 2D CrI₃ by electrostatic doping, Nat. Nanotech. **13**, 549 (2018).

[20] H. H. Kim, B Yang, T. Patel, F. Sfigakis, C. Li, S. Tian, H. Lei, and A. W. Tsen, One million percent tunnel magnetoresistance in a magnetic van der Waals heterostructure, Nano Lett. **18**, 4885 (2018).

[21] W. Jin, H. H. Kim, Z. Ye, S. Li, P. Rezaie, F. Diaz, S. Siddiq, E. Wauer, B. Yang, C. Li, S. Tian, K. Sun, H. Lei, A. W. Tsen, L. Zhao, and R. He, Raman fingerprint of two terahertz spin wave branches in a two-dimensional honeycomb Ising ferromagnet, Nat. Commun. **9**, 5122 (2018).

[22] S. Jiang, J. Shan, and K. F. Mak, Electric-field switching of two-dimensional van der Waals magnets, Nat. Mater. **17**, 406 (2018).

[23] T. Song, M. W.-Y. Tu, C. C., X. Cai, T. Taniguchi, K. Watanabe, M. A. McGuire, D. H. Cobden, D. Xiao, W. Yao, and X. Xu, Voltage control of a van der Waals spin-filter magnetic tunnel junction, Nano Lett. **19**, 915 (2019).

[24] L. Thiel, Z. Wang, M. A. Tschudin, D. Rohner, I. Gutiérrez-Lezama, N. Ubrig, M. Gibertini, E. Giannini, A. F. Morpurgo, and P. Maletinsky, Probing magnetism in 2D materials at the nanoscale with single-spin microscopy, Science **364**, 973 (2019).

[25] D. R. Klein, D. MacNeill, Q. Song, D. T. Larson, S. Fang, M. Xu, R. A. Ribeiro, P. C. Canfield, E. Kaxiras, R. Comin, and

P. Jarillo-Herrero, Enhancement of interlayer exchange in an ultrathin two-dimensional magnet, Nat. Phys. **15**, 1255 (2019).

[26] D. Soriano, A. N. Rudenko, M. I. Katsnelson, and M. Rösner, Environmental screening and ligand-field effects to magnetism in CrI₃ monolayer, npj Comput Mater **7**, 162 (2021).

[27] S. Stavrić, P. Barone, and S. Picozzi, Delving into the anisotropic interlayer exchange in bilayer CrI₃, 2D Mater. **11**, 015020 (2024).

[28] Y. Deng, Y. Yu, Y. Song, J. Zhang, N. Z. Wang, Ze. Sun, Y. Yi, Y. Z. Wu, S. Wu, J. Zhu, J. Wang, X. Hui Chen, and Y. Zhang, Gate-tunable room-temperature ferromagnetism in two-dimensional Fe₃GeTe₂, Nature (London) **563**, 94 (2018).

[29] Z. Fei, B. Huang, P. Malinowski, W. Wang, T. Song, J. Sanchez, W. Yao, D. Xiao, X. Zhu, A. F. May, W. Wu, D. H. Cobden, J.-H. Chu, and X. Xu, Two-dimensional itinerant ferromagnetism in atomically-thin Fe₃GeTe₂, Nat. Mater. **17**, 778 (2018).

[30] D. Ghazaryan, M. T. Greenaway, Z. Wang, V. H. Guarochico-Moreira1, I. J. Vera-Marun, J. Yin, Y. Liao, S. V. Morozov, O. Kristanovski, A. I. Lichtenstein, M. I. Katsnelson, F. Withers, A. Mishchenko, L. Eaves, A. K. Geim, K. S. Novoselov, and A. Misra, Magnon-assisted tunnelling in van der Waals heterostructures based on CrBr₃, Nat. Electron. **1**, 344 (2018).

[31] W. Chen, Z. Sun, Z. Wang, L. Gu, X. Xu. S. Wu, and C. Gao, Direct observation of van der Waals stacking-dependent interlayer magnetism, Science **366**, 983 (2019).

[32] A. Bedoya-Pinto, J. Ji, A. K. Pandeya, P. Gargiani, M. Valvidares, P. Sessi, J. M. Taylor, F. Radu, K. Chang, and S. S. P. Parkin, Intrinsic 2D-XY ferromagnetism in a van der Waals monolayer, Science **374**, 616 (2021).

[33] B. Karpiak, A. W. Cummings, K. Zollner, M. Vila, D. Khokhriakov, A. M. Hoque, A. Dankert, P. Svedlindh, J. Fabian, S. Roche, and S. P. Dash, Magnetic proximity in a van der Waals heterostructure of magnetic insulator and graphene, 2D Mater. **7**, 015026 (2020).

[34] K. Zollner, M. D. Petrović, K. Dolui, P. Plecháč, B. K. Nikolić, and J. Fabian, Scattering-induced and highly tunable by gate damping-like spin-orbit torque in graphene doubly proximitized by two-dimensional magnet Cr₂Ge₂Te₆ and monolayer WS₂, Phys. Rev. Res. **2**, 043057 (2020).

[35] C. Cardoso, D. Soriano, N. A. García-Martínez, and J. Fernández-Rossier, Van der waals spin valves, Phys. Rev. Lett. **121**, 067701 (2018).

[36] X.-X. Zhang, L. Li, D. Weber, J. Goldberger, K. F. Mak, and J. Shan, Gate-tunable spin waves in antiferromagnetic atomic bilayers, Nat. Mater. **19**, 838 (2020).

[37] I. A. Verzhbitskiy, H. Kurebayashi, H. Cheng, J. Zhou, S. Khan, Y. P. Feng, and G. Eda, Controlling the magnetic anisotropy in Cr₂Ge₂Te₆ by electrostatic gating, Nat. Electron. **3**, 460 (2020).

[38] W. Zhuo, B. Lei, S. Wu, F. Yu, C. Zhu, J. Cui, Z. Sun, D. Ma, M. Shi, H. Wang, W. Wang, T. Wu, J. Ying, S. Wu, Z. Wang, and X. Chen, Manipulating ferromagnetism in few-Layered Cr₂Ge₂Te₆, Adv. Mater. **33**, 2008586 (2021).

[39] F. Wu, M. Gibertini, K. Watanabe, T. Taniguchi, I. Gutiérrez-Lezama, N. Ubrig, and A. F. Morpurgo, Gate-controlled magnetotransport and electrostatic modulation of magnetism in 2D magnetic semiconductor CrPS₄, Adv. Mater. **35**, 2211653 (2023).

[40] D. Soriano and M. I. Katsnelson, Magnetic polaron and antiferromagnetic-ferromagnetic transition in doped bilayer CrI₃, Phys. Rev. B **101**, 041402(R) (2020).

[41] See, for example, A. Reserbat-Plantey, I. Epstein, I. Torre, A. T. Costa, P. A. D. Gonçalves, N. A. Mortensen, M. Polini, J. C. W. Song, N. M. R. Peres, and F. H. L. Koppens, Quantum nanophotonics in two-dimensional materials, ACS Photon. **8**, 85 (2021).

[42] S. Ghosh, G. Menichetti, M. I. Katsnelson, and M. Polini, Plasmon-magnon interactions in two-dimensional honeycomb magnets, Phys. Rev. B **107**, 195302 (2023).

[43] D. K. Efimkin and M. Kargarian, Topological spin-plasma waves, Phys. Rev. B **104**, 075413 (2021).

[44] Collective Modes of a Helical S. Raghu, S. B. Chung, X.-L. Qi, and S.-C. Zhang, Collective modes of a helical liquid, Phys. Rev. Lett. **104**, 116401 (2010).

[45] A. T. Costa, M. I. Vasilevskiy, J. Fernández-Rossier, and N. M. R. Peres, Strongly coupled magnon-plasmon polaritons in graphene-two-dimensional ferromagnet heterostructures, Nano Lett. **23**, 4510 (2023).

[46] A. Dyrdał, A. Qaiumzadeh, A. Brataas, and J. Barnaś, Magnon-plasmon hybridization mediated by spin-orbit interaction in magnetic materials, Phys. Rev. B **108**, 045414 (2023).

[47] T. Brumme, M. Calandra, and F. Mauri, Electrochemical doping of few-layer ZrNCl from first principles: Electronic and structural properties in field-effect configuration, Phys. Rev. B **89**, 245406 (2014).

[48] T. Brumme, M. Calandra, and F. Mauri, First-principles theory of field-effect doping in transition-metal dichalcogenides: Structural properties, electronic structure, Hall coefficient, and electrical conductivity, Phys. Rev. B **91**, 155436 (2015).

[49] T. Sohier, M. Calandra, and F. Mauri, Density functional perturbation theory for gated two-dimensional heterostructures: Theoretical developments and application to flexural phonons in graphene, Phys. Rev. B **96**, 075448 (2017).

[50] J. Baima, F. Mauri, and M. Calandra, Field-effect-driven half-metallic multilayer graphene, Phys. Rev. B **98**, 075418 (2018).

[51] G. F. Giuliani and G. Vignale, *Quantum Theory of the Electron Liquid* (Cambridge University Press, Cambridge, UK, 2005).

[52] G. Grosso and G. Pastori Parravicini, *Solid State Physics* (Academic Press, London, UK, 2014).

[53] G. Menichetti, M. Calandra, M. Polini, Electronic structure and magnetic properties of few-layer Cr₂Ge₂Te₆: The key role of nonlocal electron–electron interaction effects, 2D Mater. **6**, 045042 (2019).

[54] M. Wu, Z. Li, T. Cao, and S. G. Louie, Physical origin of giant excitonic and magneto-optical responses in two-dimensional ferromagnetic insulators, Nat. Commun. **10**, 2371 (2019).

[55] Y. Lee, T. Kotani, and L. Ke, Role of nonlocality in exchange correlation for magnetic two-dimensional van der Waals materials, Phys. Rev. B **101**, 241409(R) (2020).

[56] L. Ke and M. I. Katsnelson, Electron correlation effects on exchange interactions and spin excitations in 2D van der Waals materials, npj Comput. Mater. **7**, 4 (2021).

[57] F. Menescardi and D. Ceresoli, Comparative analysis of DFT+U, ACBN0, and hybrid functionals on the spin density of YTiO₃ and SrRuO₃, Appl. Sci. **11**, 616 (2021).

[58] V. I. Anisimov, J. Zaanen, and O. K. Andersen, Band theory and Mott insulators: Hubbard U instead of Stoner I, Phys. Rev. B **44**, 943 (1991).

[59] M. Cococcioni and S. de Gironcoli, Linear response approach to the calculation of the effective interaction parameters in the LDA+U method, Phys. Rev. B **71**, 035105 (2005).

[60] V. Leiria Campo Jr. and M. Cococcioni, Extended DFT +U+V method with on-site and inter-site electronic interaction, J. Phys.: Condens. Matter **22**, 055602 (2010).

[61] P. Giannozzi, S. Baroni, N. Bonini, M. Calandra, R. Car, C. Cavazzoni, D. Ceresoli, G. L. Chiarotti, M. Cococcioni, I. Dabo, A. Dal Corso, S. de Gironcoli, S. Fabris, G. Fratesi, R. Gebauer, U. Gerstmann, C. Gougoussis, A. Kokalj, M. Lazzeri, L. Martin-Samos *et al.* QUANTUM ESPRESSO: A modular and open-source software project for quantum simulations of materials, J. Phys.: Condens. Matter **21**, 395502 (2009).

[62] P. Giannozzi Jr, O. Andreussi, T. Brumme, O. Bunau, M. B. Nardelli, M. Calandra, R. Car, C. Cavazzoni, D. Ceresoli, M. Cococcioni, N. Colonna, I. Carnimeo, A. Dal Corso, S. de Gironcoli, P. Delugas, R. A. DiStasio, A. Ferretti, A. Floris, G. Fratesi, G. Fugallo, Advanced capabilities for materials modelling with QUANTUM ESPRESSO, J. Phys. Condens. Matter **29**, 465901 (2017).

[63] P. Giannozzi, O. Baseggio, P. Bonfá, D. Brunato, R. Car, I. Carnimeo, C. Cavazzoni, S. de Gironcoli, P. Delugas, F. Ferrari Ruffino, A. Ferretti, N. Marzari, I. Timrov, A. Urru, and S. Baroni, QUANTUM ESPRESSO toward the exascale, J. Chem. Phys. **152**, 154105 (2020).

[64] R. Dovesi, R. Orlando, A. Erba, C. M. Zicovich-Wilson, B. Civalleri, L. Maschio, M. Rerat, S. Casassa, J. Baima, S. Salustro, and B. Kirtman, Quantum-mechanical condensed matter simulations with CRYSTAL, WIREs Comput. Mol. Sci. **8**, e1360 (2018).

[65] R. Dovesi, R. Orlando, A. Erba, C. M. Zicovich-Wilson, B. Civalleri, S. Casassa, L. Maschio, M. Ferrabone, M. De La Pierre, P. D'Arco, Y. Noel, M. Causa, M. Rerat, and B. Kirtman, CRYSTAL14: A program for the *ab initio* investigation of crystalline solids, Int. J. Quantum Chem. **114**, 1287 (2014).

[66] D. R. Hamann, Optimized norm-conserving Vanderbilt pseudopotentials, Phys. Rev. B **88**, 085117 (2013).

[67] M. Schlipf and F. Gygi, Optimization algorithm for the generation of ONCV pseudopotentials, Comput. Phys. Commun. **196**, 36 (2015).

[68] P. Scherpelz, M. Govoni, I. Hamada, and G. Galli, Implementation and validation of fully relativistic GW calculations: Spin–orbit coupling in molecules, nanocrystals, and solids, J. Chem. Theory Comput. **12**, 3523 (2016).

[69] J. Heyd, G. E. Scuseria, and M. Ernzerhof, Hybrid functionals based on a screened Coulomb potential, J. Chem. Phys. **118**, 8207 (2003).

[70] J. P. Perdew, K. Burke, and M. Ernzerhof, Generalized gradient approximation made simple, Phys. Rev. Lett. **77**, 3865 (1996).

[71] S. Grimme, Semiempirical GGA-type density functional constructed with a long-range dispersion correction, J. Comput. Chem. **27**, 1787 (2006).

[72] N. Marzari, D. Vanderbilt, A. De Vita, and M. C. Payne, Thermal contraction and disordering of the Al(110) surface, Phys. Rev. Lett. **82**, 3296 (1999).

[73] H. J. Monkhorst and J. D. Pack, Special points for Brillouin-zone integrations, Phys. Rev. B **13**, 5188 (1976).

[74] M. Catti, G. Sandrone, G. Valerion and R. Dovesi, Electronic, magnetic and crystal structure of Cr_2O_3 by theoretical methods, J. Phys. Chem. Solids **57**, 1735 (1996).

[75] J. Heyd, J. E. Peralta, G. E. Scuseria, and R. L. Martin, Energy band gaps and lattice parameters evaluated with the Heyd-Scuseria-Ernzerhof screened hybrid functional, J. Chem. Phys. **123**, 174101 (2005).

[76] A. A. Mostofi, J. R. Yates, G. Pizzi, Y. S. Lee, I. Souza, D. Vanderbilt, and N. Marzari, An updated version of wannier90: A tool for obtaining maximally localised Wannier functions, Comput. Phys. Commun. **185**, 2309 (2014).

[77] N. Marzari and D. Vanderbilt, Maximally localized generalized Wannier functions for composite energy band, Phys. Rev. B **56**, 12847 (1997).

[78] I. Souza, N. Marzari, and D. Vanderbilt, Maximally localized Wannier functions for entangled energy bands, Phys. Rev. B **65**, 035109 (2001).

[79] K. Momma and F. Izumi, *VESTA* 3 for three-dimensional visualization of crystal, volumetric and morphology data, J. Appl. Crystallogr. **44**, 1272 (2011).

[80] A. Kokalj, Computer graphics and graphical user interfaces as tools in simulations of matter at the atomic scale, Comput. Mater. Sci. **28**, 155 (2003).

[81] V. Carteaux, B. Brunet, G. Ouvrard, and G. Andre, Magnetic and electronic structures of a new layered ferromagnetic compound $Cr_2Ge_2Te_6$, J. Phys.: Condens. Matter **7**, 69 (1995).

[82] B. Siberchicot, S. Jobic, V. Carteaux, P. Gressier, and G. Ouvrard, Band structure calculations of ferromagnetic chromium tellurides $CrSiTe_3$ and $CrGeTe_3$, J. Phys. Chem. **100**, 5863 (1996).

[83] J. B. Goodenough, Theory of the role of covalence in the perovskite-type manganites [La, M(II)]MnO_3, Phys. Rev. **100**, 564 (1955).

[84] J. Kanamori, Superexchange interaction and symmetry properties of electron orbitals, J. Phys. Chem. Solids **10**, 87 (1959).

[85] M. D. Watson, I. Marković, F. Mazzola, A. Rajan, E. A. Morales, D. M. Burn, T. Hesjedal, G. van der Laan, S. Mukherjee, T. K. Kim, C. Bigi, I. Vobornik, M. Ciomaga Hatnean, G. Balakrishnan, and P. D. C. King, Direct observation of the energy gain underpinning ferromagnetic superexchange in the electronic structure of $CrGeTe_3$, Phys. Rev. B **101**, 205125 (2020).

[86] V. A. Gubanov, A. I. Liechtenstein, and A. V. Postnikov, *Magnetism and the Electronic Structure of Crystals* (Springer-Verlag, Berlin-Heidelberg, 1992).

[87] A. Auerbach, *Interacting Electrons and Quantum Magnetism* (Springer-Verlag, New York, NY, 1994).

[88] N. D. Mermin and H. Wagner, Absence of ferromagnetism or antiferromagnetism in one- or two-dimensional isotropic Heisenberg models, Phys. Rev. Lett. **17**, 1133 (1966).

[89] D. Torelli and T. Olsen, Calculating critical temperatures for ferromagnetic order in two-dimensional materials, 2D Mater. **6**, 015028 (2019).

[90] P. Bruno, Tight-binding approach to the orbital magnetic moment and magneto-crystalline anisotropy of transition-metal monolayers, Phys. Rev. B **39**, 865 (1989).

[91] D. Li, C. Barreteau, M. R. Castell, F. Silly, and A. Smogunov, Out- versus in-plane magnetic anisotropy of free Fe and Co nanocrystals: Tight-binding and first-principles studies, Phys. Rev. B **90**, 205409 (2014).

[92] Z. Li, T. Cao, and S. G. Louie, Two-dimensional ferromagnetism in few-layer van der Waals crystals: Renormalized spin-wave theory and calculations, J. Magn. Magn. Mater. **463**, 28 (2018).

[93] T. Moriya, Anisotropic superexchange interaction and weak ferromagnetism, Phys. Rev. **120**, 91 (1960).

[94] S. I. Vishkayi, Z. Torbatian, A. Qaiumzadeh, and R. Asgari, Strain and electric-field control of spin-spin interactions in monolayer CrI_3, Phys. Rev. Mater. **4**, 094004 (2020).

[95] M.-H. Whangbo, H.-J. Koo, and D. Dai, Spin exchange interactions and magnetic structures of extended magnetic solids with localized spins: Theoretical descriptions on formal, quantitative and qualitative levels, J. Solid State Chem. **176**, 417 (2003).

[96] H. J. Xiang, E. J. Kan, S.-H. Wei, M.-H. Whangbo, and X. G. Gong, Predicting the spin-lattice order of frustrated systems from first principles, Phys. Rev. B **84**, 224429 (2011).

[97] H. Xiang, C. Lee, H.-J. Koo, X. Gong, and M.-H. Whangbo, Magnetic properties and energy-mapping analysis, Dalton Trans. **42**, 823 (2013).

[98] D. Šabani, C. Bacaksiz, and M. V. Milošević, *Ab initio* methodology for magnetic exchange parameters: Generic four-state energy mapping onto a Heisenberg spin Hamiltonian, Phys. Rev. B **102**, 014457 (2020).

[99] We also have reached a converged value of J_4 in a $\sqrt{13} \times \sqrt{13}$ super-cell.

[100] C. Zener, Interaction between the d-Shells in the transition metals. II. Ferromagnetic compounds of manganese with perovskite structure, Phys. Rev. **82**, 403 (1951).

[101] D. N. Aristov, Indirect RKKY interaction in any dimensionality, Phys. Rev. B **55**, 8064 (1997).

[102] V. I. Litvinov and V. K. Dugaev, RKKY interaction in one- and two-dimensional electron gases, Phys. Rev. B **58**, 3584 (1998).

[103] The RKKY interaction between two localized moments can be written as $\mathcal{H}_{\text{RKKY}} = -A^2 S_1 S_2 \widetilde{\chi}(\boldsymbol{R}_{12})/2$. Here, A is an interaction constant, $\boldsymbol{R}_{12}$ is the distance between the localized spins, and $\widetilde{\chi}(\boldsymbol{R}_{12})$ is the Fourier transform of the static density-density response function $\chi(\boldsymbol{q})$ (also known as "Lindhard function" [51]). In the present case, we have employed the density-density of a uniform non-interacting 2D electron gas [51], using m_{h}^* as band mass.

[104] D. Zhang, A. Rahman, W. Qin, X. Li, P. Cui, Z. Zhang, and Z. Zhang, Prediction of $MnSiTe_3$ as an intrinsic layered half-metal, Phys. Rev. B **101**, 205119 (2020).

[105] C. Tang, K. Ostrikov, S. Sanvito, and A. Du, Prediction of room-temperature ferromagnetism and large perpendicular magnetic anisotropy in a planar hypercoordinate FeB_3 monolayer, Nanoscale Horiz. **6**, 43 (2021).